

# The size of the X–ray emitting region in SWIFT J2127.4+5654 via a broad line region cloud X–ray eclipse

M. Sanfrutos<sup>1\*</sup>, G. Miniutti<sup>1</sup>, B. Agís-González<sup>1</sup>, A. C. Fabian<sup>2</sup>, J. M. Miller<sup>3</sup>,  
F. Panessa<sup>4</sup> and A. Zoghbi<sup>5,6</sup>

<sup>1</sup> Centro de Astrobiología (CSIC–INTA), Dep. de Astrofísica; ESA, P.O: Box 78, E-28691, Villanueva de la Cañada, Madrid, Spain

<sup>2</sup> Institute of Astronomy, Madingley Road, Cambridge CB3 0HA

<sup>3</sup> Department of Astronomy, University of Michigan, 500 Church St., Ann Arbor, MI48109, USA

<sup>4</sup> INAF - Istituto di Astrofisica e Planetologia Spaziali di Roma (IAPS), Via del Fosso del Cavaliere 100, 00133 Roma, Italy

<sup>5</sup> Department of Astronomy, University of Maryland, College Park, MD 20742-2421, USA

<sup>6</sup> Joint Space-Science Institute (JSI), College Park, MD 20742-2421, USA

16 October 2018

## ABSTRACT

We present results obtained from the time–resolved X–ray spectral analysis of the Narrow–Line–Seyfert 1 galaxy SWIFT J2127.4+5654 during a  $\sim 130$  ks *XMM–Newton* observation. We reveal large spectral variations, especially during the first  $\sim 90$  ks of the *XMM–Newton* exposure. The spectral variability can be attributed to a partial eclipse of the X–ray source by an intervening low–ionization/cold absorbing structure (cloud) with column density  $N_{\text{H}} = 2.0^{+0.2}_{-0.3} \times 10^{22} \text{ cm}^{-2}$  which gradually covers and then uncovers the X–ray emitting region with covering fraction ranging from zero to  $\sim 43$  per cent. Our analysis enables us to constrain the size, number density, and location of the absorbing cloud with good accuracy. We infer a cloud size (diameter) of  $D_{\text{c}} \leq 1.5 \times 10^{13} \text{ cm}$ , corresponding to a density of  $n_{\text{c}} \geq 1.5 \times 10^9 \text{ cm}^{-3}$  at a distance of  $R_{\text{c}} \geq 4.3 \times 10^{16} \text{ cm}$  from the central black hole. All of the inferred quantities concur to identify the absorbing structure with one single cloud associated with the broad line region of SWIFT J2127.4+5654. We are also able to constrain the X–ray emitting region size (diameter) to be  $D_{\text{s}} \leq 2.3 \times 10^{13} \text{ cm}$  which, assuming the black hole mass estimated from single–epoch optical spectroscopy ( $1.5 \times 10^7 M_{\odot}$ ), translates into  $D_{\text{s}} \leq 10.5$  gravitational radii ( $r_{\text{g}}$ ) with larger sizes (in  $r_{\text{g}}$ ) being associated with smaller black hole masses, and viceversa. We also confirm the presence of a relativistically distorted reflection component off the inner accretion disc giving rise to a broad relativistic Fe K emission line and small soft excess (small because of the high Galactic column density), supporting the measurement of an intermediate black hole spin in SWIFT J2127.4+5654 that was obtained from a previous *Suzaku* observation.

**Key words:** galaxies: active – X-rays: galaxies

## 1 INTRODUCTION

X–ray flux and spectral variability is a rather common property of Active Galactic Nuclei (AGN). Spectral variability on relatively long timescales (months to years) is often associated with absorption variability (e.g. Warwick et al. 1988; Risaliti et al. 2002; Marinucci et al. 2012). In recent years, several examples of short–timescale (hours to days) absorption variability have been reported (e.g. NGC 4388, Elvis et al. 2004; NGC 4151, Puccetti et al. 2007; NGC 1365, Risaliti et al. 2005; 2007; 2009 and Maiolino et al. 2010; NGC 7582, Bianchi et al. 2009; Mrk 766).

The detailed analysis of the short–timescale absorption variability in these sources strongly suggests the presence of absorbing structures (clouds) crossing the line–of–sight to a rather compact X–ray source. The data are generally consistent with the presence of an ensemble of compact, cold clouds with typical column density of  $10^{22} - 10^{24} \text{ cm}^{-2}$ , density of  $10^9 - 10^{11} \text{ cm}^{-3}$ , velocity of few times  $10^3 \text{ km s}^{-1}$ , and distance of  $10^2 - 10^4 r_{\text{g}}$  from the centre. These properties are remarkably similar to those of the clouds responsible for the emission of the broad optical and UV emission lines in AGN. Hence, X–ray absorption variability studies suggest to identify the X–ray compact absorbers responsible for the shortest timescale absorption variability events with broad line region (BLR) clouds, while variability on longer timescales (months to

\* sanfrutoscm@cab.inta-csic.es

years) is likely associated with more extended structures, possibly associated with a clumpy torus (Nenkova et al. 2008). Here we report results from a  $\sim 130$  ks observation of the Narrow Line Seyfert 1 galaxy SWIFT J2127.4+5654 with *XMM-Newton*.

SWIFT J2127.4+5654 (a.k.a. IGR J21277+5656) is a low Galactic latitude hard X-ray source which has been first detected at hard X-rays with *Swift*/BAT (Tueller et al. 2005). Later, the source was identified as a Narrow-Line Seyfert 1 (NLS1) galaxy at redshift 0.0147 based on the observed  $H\alpha$  FWHM of  $\sim 1180$  km/s (Halpern 2006). Subsequent work by Malizia et al. (2008) supported the NLS1 classification by obtaining, despite a slightly larger FWHM of  $\sim 2000$  km/s, a relatively low  $[O\ III]/H\beta$  ratio of  $0.72 \pm 0.05$  and significantly enhanced Fe II emission ( $Fe\ II/H\beta = 1.3 \pm 0.2$ ). SWIFT J2127.4+5654 was then observed with *Suzaku* for a total net exposure of 92 ks and results have been presented and discussed by Miniutti et al. (2009). The major result of the *Suzaku* observation is the detection of a relativistically broadened Fe  $K\alpha$  emission line which strongly suggests that SWIFT J2127.4+5654 is powered by accretion onto a rotating Kerr black hole, with an intermediate spin value of  $a = 0.6 \pm 0.2$ . This result has been confirmed (using the same data set) also by Patrick et al. (2010) who report  $a = 0.70^{+0.10}_{-0.14}$ , although a different interpretation of the Fe  $K\alpha$  shape, based on reprocessing and scattering in a Compton-thick disc-wind rather than the disc itself, has also been proposed (Tatum et al. 2012).

## 2 X-RAY OBSERVATIONS

*XMM-Newton* observed SWIFT J2127.4+5654 on 2010 November 29 for a full revolution ( $\sim 130$  ks). The observation (0655450101) was performed using the Small Window mode for all EPIC cameras, with the optical thin filter applied. The data were reduced as standard using the dedicated SAS v11.0 software. Observation-dependent EPIC and RGS response files were generated using the RMFGEN and ARFGEN tasks. EPIC source products were extracted from circular regions of  $40''$  centred on the source, and the corresponding background was estimated by using source-free nearby regions. In the time-resolved analysis we present in this work, each time-interval is associated with its own background spectrum contributing less than 2 per cent in any of the considered time-intervals. After filtering for high background periods which occur at the beginning and end of the exposure, the net exposure is  $\sim 84$  ks in the EPIC-pn spectrum and  $\sim 109$  ks and  $\sim 110$  ks in the MOS 1 and MOS 2 spectra respectively. All the EPIC spectra are extracted with common good-time-intervals and they are all grouped in order to guarantee that each background-subtracted bin has at least 25 counts.

The MOS and pn spectra are consistent with each other above  $\sim 1.6$  keV. However, as shown in the upper panel of Fig. 1, the spectra are not consistent with each other at softer energies. The largest discrepancies are between the pn and the two MOS detectors below 1.6 keV and between the two MOS cameras below 0.9 keV. In the lower panel, we plot the RGS 2 data-to-model ratio instead of the EPIC pn. The RGS spectrum confirms the reliability of the MOS data above 0.9 keV and suggests to ignore the pn softest data. Moreover, the spectral shape in the previous *Suzaku* observation (Miniutti et al. 2009) agrees much better with the MOS/RGS spectra than with the pn one. This comparative analysis suggests to make a conservative choice of the energy ranges to be used for spectral analysis. In our work we consider the MOS data in the 0.9–10 keV band, and the pn data in the 1.6–10 keV

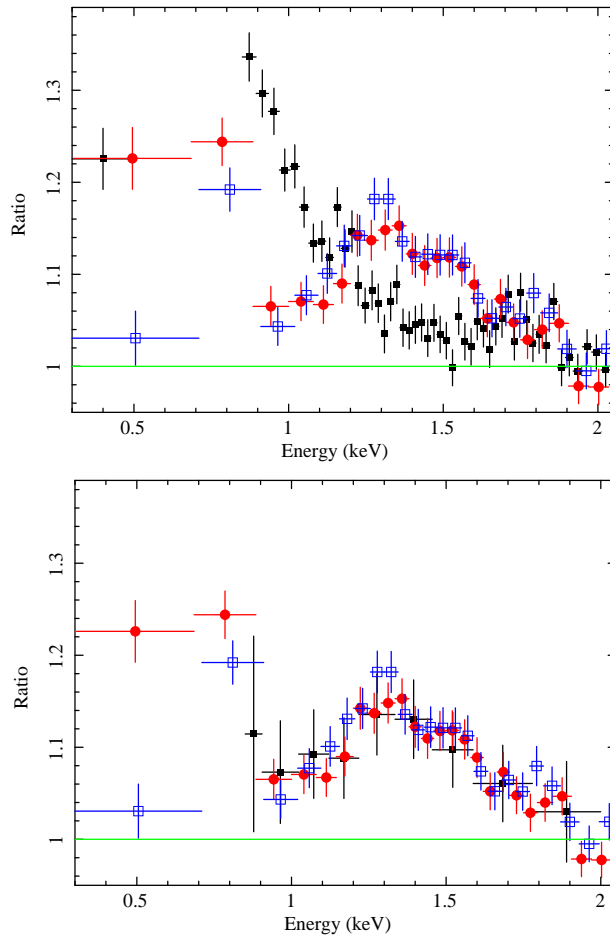


**Figure 1.** In the upper panel, we show a comparison between the EPIC pn (filled black squares), MOS 1 (filled circles, red in the on-line version), and MOS 2 (empty squares, blue in the on-line version) spectra in the soft X-ray band. All spectra are fitted in the 2–4 keV and 7.5–10 keV band (i.e. ignoring the Fe K band) with a common spectral model comprising Galactic absorption and a power law. See the upper panel of Fig. 2 for a comparison between the pn and MOS data at higher energies using the same spectral model used here. In the lower panel, we show the same MOS data as above, but we plot the (heavily rebinned) RGS 2 data-to-model ratio instead of the EPIC pn (we omit the RGS 1 data here because of the gap around the crucial 0.9–1.1 keV band affecting the RGS 1 detector). The RGS data below 0.8–0.9 keV are too noisy to be used for this comparison.

band. Our choice of reliable energy bands to be used for the spectral analysis is in fact very conservative, and we have checked a-posteriori that almost exactly the same results on the most relevant best-fitting parameters are obtained considering all data in the 0.5–10 keV band, although with worse statistical results due to the discrepancies between the pn and the MOS spectra. In any case, it should also be mentioned that, since the low Galactic latitude of SWIFT J2127.4+5654 corresponds to a relatively high Galactic column density ( $7.65 \times 10^{21} \text{ cm}^{-2}$ , Kalberla et al. 2005), soft X-ray data below 1 keV only provide  $\sim 7$  per cent of the total collected counts, with very little impact on the overall analysis. When needed to convert fluxes into luminosities, we adopt a cosmology with  $H_0 = 70 \text{ km s}^{-1} \text{ Mpc}^{-1}$ ,  $\Omega_\Lambda = 0.73$ , and  $\Omega_M = 0.27$ .

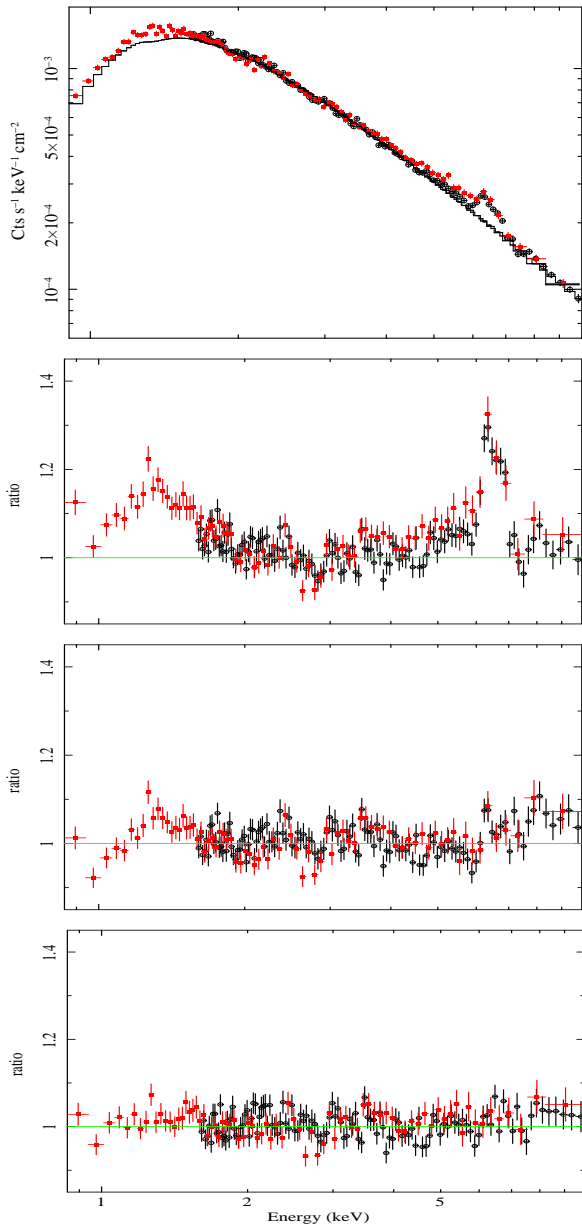


**Figure 2.** In the upper panel, we show the EPIC pn (empty circles) and MOS 1 data (filled squares, red in the on-line version) divided by the detector effective area to show the real spectral shape, together with the best-fitting power law model fitted in the 2–4 keV and 7.5–10 keV data. Although the MOS 2 data were also used in the spectral analysis in the 0.9–10 keV band, they are omitted here for visual clarity. In the second panel, we show the resulting data-to-model ratio. In the third panel, we show the data-to-model ratio resulting from including a relativistically blurred Fe emission line. In the lower panel we show the final best-fitting model comprising a relativistically blurred reflection model plus a series of narrow emission lines as detailed in the text.

### 3 THE TIME-AVERAGED SPECTRUM

We start our analysis by considering the time-averaged X-ray spectrum of SWIFT J2127.4+5654 in the 0.9–10 keV band using all EPIC detectors. In the upper two panels of Fig. 2 we show the data-to-model ratio resulting from a simple absorbed power law model fitted in the 2–4 keV and 7.5–10 keV, i.e. ignoring the Fe K band (as mentioned, we use the MOS data in the 0.9–10 keV band,

and the pn data in the 1.6–10 keV band). Absorption is here modelled with only the Galactic column density of  $7.65 \times 10^{21} \text{ cm}^{-2}$  (Kalberla et al. 2005). The continuum is modelled with a power law of  $1.81 \pm 0.02$ . The model leaves significant residuals around the Fe K band, where a broad feature reminiscent of a relativistic broad Fe line is seen, and below  $\sim 2$  keV where a soft X-ray excess is detected.

We then add a relativistic Fe line using the KERRCONV relativistic convolution model from Brenneman & Reynolds (2006) applied to a 6.4 keV Gaussian emission line with zero intrinsic width. The statistical description of the data is relatively good with  $\chi^2 = 4080$  for 3838 degrees of freedom (dof). Adding an intrinsic neutral absorber at the redshift of the source improves the statistic to  $\chi^2 = 4030$  for 3837 dof. The nature and properties of the absorber will be discussed in detail in subsequent Sections. Here we only mention that we obtain a column density of  $\sim 2 \times 10^{21} \text{ cm}^{-2}$  in addition to the Galactic one. The resulting data-to-model ratio is shown in the third panel of Fig. 2. Some residuals are still present in the soft and hard bands.

As the detected broad line should be associated with a disc reflection continuum, we replace the relativistic line model with a full disc reflection model from partially ionized gas (Ross & Fabian 2005) to which we apply the same relativistic convolution model as before. The model describes the data better with 3976 for 3836 dof, and accounts for both the soft and hard residuals seen in the middle panel of Fig. 2.

Further residuals are however left around the Fe K band, suggesting the presence of a series of narrow emission lines. We find that four narrow lines are indeed required by the data. Their energy is consistent with 6.4 keV (Fe K $\alpha$ ), 6.7 keV (Fe xxv Ly $\alpha$ ), 6.97 keV (Fe xxvi Ly $\alpha$ ), and 8.25 keV (Fe xxvi Ly $\beta$ ) so that we fix their energy at the theoretical values. The statistical improvement for the inclusion of these additional narrow lines is  $\Delta\chi_{6.4}^2 = -22$ ,  $\Delta\chi_{6.7}^2 = -11$ ,  $\Delta\chi_{6.97}^2 = -10$ , and  $\Delta\chi_{8.25}^2 = -7$ , where each line contributes with one additional degree of freedom only (its normalization). Only the narrow Fe K $\alpha$  emission line was detected during the previous *Suzaku* observation. However, the 2–10 keV flux was a factor of  $\sim 2$  higher than during the *XMM-Newton* observation, which can easily explain the non-detection of the ionized Fe lines as, for constant-intensity lines, their EW drops by a similar factor and becomes consistent with zero within the uncertainties. This likely signals that the ionized lines are associated with emission from extended photo-ionized gas, so that their flux remains constant and the lines can only be detected when the X-ray continuum flux is relatively low, as during the *XMM-Newton* observation. The same applies to the narrow Fe K $\alpha$  line at 6.4 keV, as its EW during the *Suzaku* observation ( $13 \pm 9$  eV) is broadly consistent with being half of that measured here ( $\sim 50 \pm 17$  eV), which is what is expected for a line with a constant intensity and a continuum variation by a factor of  $\sim 2$ . We point out that if the width of the Fe K $\alpha$  line is allowed to vary during the fit, we have  $\sigma \leq 0.1$  keV, corresponding to a FWHM  $\leq 1.1 \times 10^4 \text{ km s}^{-1}$  (consistent with any production site, from the innermost BLR outwards). With the addition of these narrow emission lines, the final best-fitting model for the 0.9–10 keV spectrum produces a statistical result of 3926 for 3832 dof. The best-fitting data-to-model ratio is shown in the lower panel of Fig. 2. The most important best-fitting parameters are reported in Table 1. All relativistic parameters (emissivity index, black hole spin, disc inclination) are consistent with the results of Miniutti et al. (2009) who measured  $q \sim 5.3$ ,  $a \sim 0.6$  and  $i \sim 46^\circ$  from the previous *Suzaku* observation. The good agreement between the *XMM-Newton* and *Suzaku*

**Table 1.** Best-fitting parameters from the time-averaged 0.9–10 keV spectral analysis of SWIFT J2127.4+5654. The column density of the intrinsic absorber at the redshift of the source is in units of  $10^{22} \text{ cm}^{-2}$ . The reflector ionization state is given in units of  $\text{erg cm s}^{-1}$ . The 2–10 keV flux is in units of  $10^{-11} \text{ erg cm}^{-2} \text{ s}^{-1}$  and is as observed, while the 2–10 keV luminosity is unabsorbed and expressed in  $10^{42} \text{ erg s}^{-1}$ . The equivalent widths (EW) are expressed in units of eV and they refer to the narrow emission lines at 6.4 keV (Fe K $\alpha$ ), 6.7 keV (Fe xxv Ly $\alpha$ ), 6.97 keV (Fe xxvi Ly $\alpha$ ), and 8.25 keV (Fe xxvi Ly $\beta$ ).

$\Gamma$	.....	$2.00 \pm 0.04$
$N_{\text{H}}$	.....	$0.2 \pm 0.1$
$q$	.....	$4.9 \pm 0.9$
$a$	.....	$0.5 \pm 0.3$
$i$	.....	$44^\circ \pm 8^\circ$
$\xi_{\text{ref}}$	.....	$10 \pm 6$
$EW_{6.4}$	.....	$50 \pm 17$
$EW_{6.7}$	.....	$23 \pm 11$
$EW_{6.97}$	.....	$25 \pm 10$
$EW_{8.25}$	.....	$18 \pm 14$
$F_{2-10}$	.....	$1.90 \pm 0.04$
$L_{2-10}$	.....	$9.6 \pm 0.2$
$\chi^2/\text{dof}$	.....	$3926/3832$

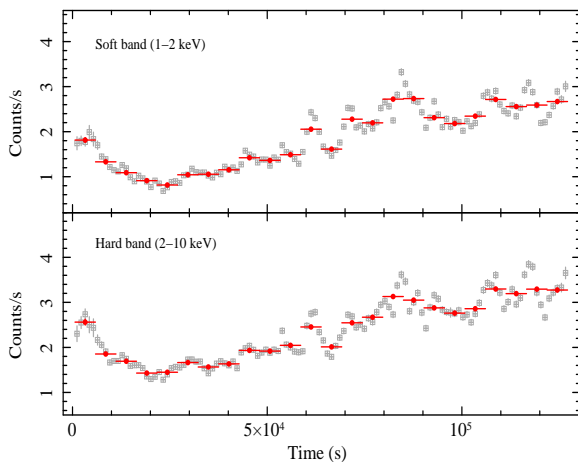


**Figure 3.** The soft (S: 1–2 keV, upper) and hard (H: 2–10 keV, lower) X-ray light curves of SWIFT J2127.4+5654 from the pn detector are shown in bins of 500 s (empty grey squares) and 5271.8 s (filled red circles). The latter bin-size is chosen to divide the total exposure in 24 uniform time-intervals which will be used to perform a time-resolved spectral analysis of the data.

data provides independent support to the interpretation of the spectral shape in terms of relativistically distorted disc reflection, as originally proposed by Miniutti et al. (2009).

#### 4 SPECTRAL VARIABILITY

As already shown in previous work (e.g. Miniutti et al. 2009), SWIFT J2127.4+5654 is highly variable in X-rays, an almost ubiquitous property of NLS1 galaxies. X-ray flux variability is also present in the *XMM-Newton* observation. In Fig. 3, we show the EPIC-pn light curve in a soft (S: 1–2 keV) and a hard (H: 2–

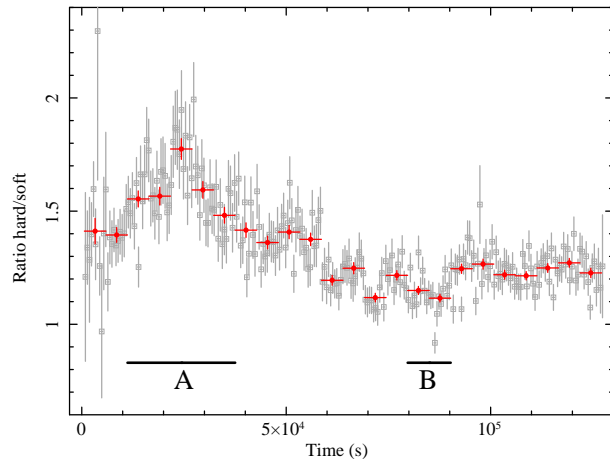


**Figure 4.** The hard-to-soft ratio (H/S) light curve of SWIFT J2127.4+5654 from the pn detector is shown with the same bin-size as in Fig. 3. SWIFT J2127.4+5654 exhibits highly significant spectral variability during the first  $\sim 90$  ks, while H/S remains approximately constant during the subsequent  $\sim 35$  ks. We also highlight the two intervals of highest (A) and lowest (B) H/S that are used in the spectral variability analysis (see text for details).

10 keV) band<sup>1</sup>. The source is variable on all probed timescales and exhibits variability up to a factor of  $\sim 4$  during the *XMM-Newton* exposure. Significant bin-to-bin variability is present down to the chosen bin-size of 500 s, with more than one third of any two consecutive bins being inconsistent with each other. We then consider the hard-to-soft ratio (H/S) light curve, to investigate whether spectral variability is also present during the observation. The H/S light curve is shown in Fig. 4 with the same bin-size as in Fig. 3. Clear spectral variability is present in the first  $\sim 90$  ks of the exposure, while H/S remains approximately stable in the subsequent  $\sim 35$  ks.

#### 4.1 Time-resolved analysis and spectral variability

In order to understand the origin of the spectral variability, we first extract X-ray spectra from the two time-intervals, denoted as A and B in Fig. 4, which correspond to the highest and lowest H/S ( $1.59^{+0.24}_{-0.15}$  and  $1.13 \pm 0.04$  respectively). The different duration of intervals A and B is justified by the different flux levels, and by the requirement that the two spectra share a similar spectral quality (i.e. that the spectra have similar number of counts). Interval A is  $\sim 26$  ks long and corresponds to a 0.9–10 keV flux of  $\sim 1.46 \times 10^{-11} \text{ erg cm}^{-2} \text{ s}^{-1}$ , while interval B is  $\sim 11$  ks long with a flux of  $\sim 2.83 \times 10^{-11} \text{ erg cm}^{-2} \text{ s}^{-1}$  in the same band. Visual inspection of spectra A and B shows that the two spectra only differ spectrally below  $\sim 3$ –4 keV where spectrum A has a deficit of soft photons, possibly the signature of extra-absorption with respect to the lower H/S spectrum B.

The spectra from intervals A and B are fitted jointly with the best-fitting model inferred from the time-averaged spectral analysis. We fix the relativistic parameters to their time-averaged best-

<sup>1</sup> We extend the EPIC pn energy range down to 1 keV although we only use the pn data above 1.6 keV in our spectral analysis, as light curves and, even more so, hardness ratios are reasonably calibration-independent. The shape of the pn light curves shown in Fig. 3 and Fig. 4 has been checked against the MOS data which confirm that the EPIC pn light curves are reliable.

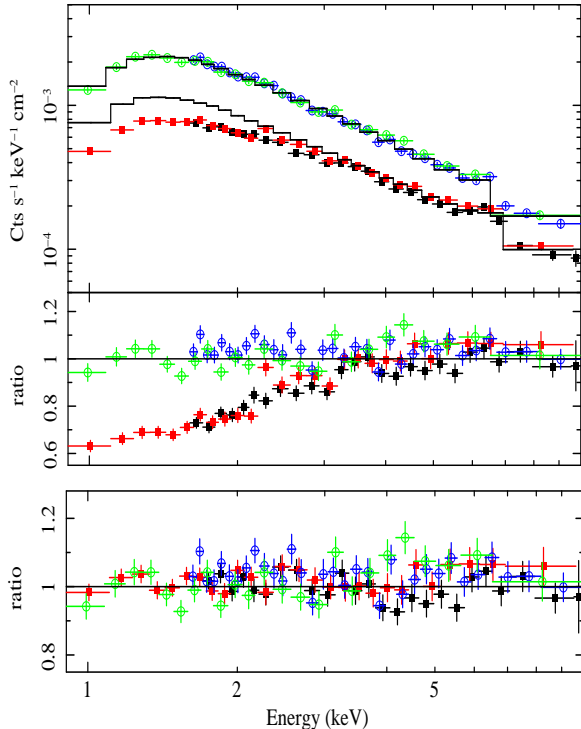


**Figure 5.** In the upper panel we show the data divided by the appropriate detector effective area, best-fitting models, and data-to-model ratio for spectra A (lower two spectra, filled squares, black and red in the on-line version for the pn and MOS 1 cameras respectively) and B (upper two spectra, empty circles, blue and green in the on-line version for the pn and MOS 1 cameras respectively). The MOS 2 data are also used in the analysis in the 0.9–10 keV band (as for the MOS 1 data) but are not shown here for visual clarity. The spectral model is fitted only above 3.5 keV and then extrapolated to soft energies to show the significant spectral difference between the two time-intervals. In the lower panel, we show the final best-fitting data-to-model ratio where the spectra A residuals are accounted for by an additional neutral absorber only partially covering the X-ray continuum (see text for details).

fitting values, as the lower quality of the time-resolved spectra does not allow us to better constrain them. We also fix the normalization of all the narrow emission lines to their time-averaged best-fitting values as these components are not expected to vary on short timescales. We start our analysis by considering only the data above 3.5 keV. We initially allow for possible variation in the continuum photon index  $\Gamma$ . However, as  $\Gamma$  turns out to be consistent with being constant, we force it to be the same in the A and B spectra. We reach an excellent description of the hard X-ray spectra of intervals A and B at energies above 3.5 keV with  $\chi^2 = 1190$  for 1196 dof. However, the extrapolation to soft energies reveals a large spectral difference between the two intervals, as shown in the upper panel of Fig. 5. The spectrum from interval A appear to be significantly more absorbed than that from interval B, as already suggested by the H/S difference between the two time-intervals in Fig. 4.

We then add a layer of absorbing gas to our model. We use a partial covering model for neutral gas (the ZPCFABS model). In principle, both the column density and the covering fraction may be variable. However, due to the relatively low quality of the data, the two parameters cannot be constrained independently. In order to explain physically the short-timescale spectral variability, we assume that the absorber column density is the same in both spec-

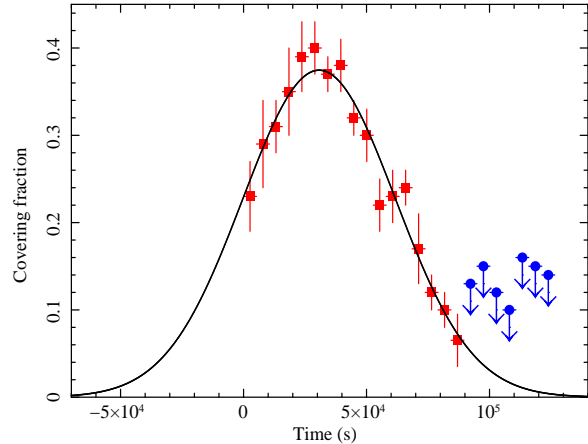


**Figure 6.** The covering fraction ( $CF$ ) evolution during the *XMM-Newton* observation. Significant  $CF$  variability is present in the first  $\sim 90$  ks. Our results indicate that the X-ray continuum is partially absorbed during the first 90 ks of the exposure by a column density of  $\sim 2 \times 10^{22} \text{ cm}^{-2}$  with variable  $CF$ , while the data are consistent with the X-ray continuum being unabsorbed thereafter. The solid curve represents a simple Gaussian model for the  $CF$  evolution during the first  $\sim 90$  ks.

trum A and B, while its covering fraction is allowed to vary independently. The model provides an excellent description of the data ( $\chi^2 = 3179$  for 3135 dof). In the lower panel of Fig. 5 we show the resulting best-fitting data-to-model ratio for the spectra A and B. The observed variability between intervals A and B can be entirely explained by a layer of neutral absorbing gas with column density  $N_{\text{H}} = 2.0_{-0.5}^{+0.6} \times 10^{22} \text{ cm}^{-2}$  covering  $\sim 35$  per cent of the X-ray source during interval A and  $\leq 4$  per cent during interval B. If the photon indices of spectra A and B are now allowed to vary independently, no further statistical improvement is obtained, and the two spectral slopes are consistent with each other.

## 4.2 A partial eclipse

We then consider the spectral variability of SWIFT J2127.4+5654 on shorter timescales within the framework of the partial covering model. We extract 24 spectra (for each of the EPIC cameras) from intervals of equal duration (i.e. from the 5271.8 s long intervals shown in Fig. 4), and we apply the same model discussed above to all spectra. We force all parameters to be the same, except the power law normalisation, the reflector ionization<sup>2</sup>, and the absorber covering fraction. The overall fit is excellent (reduced  $\chi^2 = 0.98$ ), and we obtain a common absorber column density of  $N_{\text{H}} = 2.0_{-0.3}^{+0.2} \times 10^{22} \text{ cm}^{-2}$ , consistent with that derived above from the analysis of intervals A and B.

The covering fraction ( $CF$ ) during the different intervals is clearly variable, and its evolution is shown in Fig. 6. The evolution during the first 90 ks of the exposure is smooth and can be roughly

<sup>2</sup> We impose the same reflection normalization in all spectra. This is because, by definition, two reflection models with the same normalization and illuminating power law slope but with different ionization parameters satisfy a linear relation between ionization and total reflection flux, see e.g. Miniutti et al. 2012. Imposing that this is the case by forcing all reflection normalization to be the same increases the overall self-consistency of the model, as the two quantities are both linearly correlated with the flux irradiating the disc. It also helps lowering the number of free parameters in the model, reducing the risk of over-modelling data of relatively poor quality.

described by a Gaussian-like shape, while SWIFT J2127.4+5654 is consistent with being unabsorbed thereafter. The Gaussian-like shape of the covering fraction variability suggests that one single absorbing structure (cloud) with size similar to that of the X-ray source has crossed the line-of-sight during the first 90 ks of the observation. Below, we discuss the implications of the main event that characterises the first 90 ks of the observation, and we derive the properties of the absorber as well as the size of the X-ray emitting region. Here we simply point out that the intrinsic absorber detected in the time-averaged spectrum (see section 3) is just the flux-weighted average of the absorption column density and  $CF$  during the whole exposure, so that little physical meaning should be attached to the derived column density in the time-averaged spectral analysis.

## 5 CLOUD PROPERTIES AND THE X-RAY EMITTING REGION SIZE

The behaviour of the covering fraction data in Fig. 6, identifies three phases during the eclipse: a fast rise of CF from zero to maximal CF ( $\sim 35 - 45$  per cent), a flat plateau with maximal CF, and finally a decaying phase from maximal CF to zero. The existence of a plateau with maximal CF smaller than 1, as well as the steepness of the rising and decaying phases, point towards a physical situation characterised by a cloud, smaller than the source, crossing our line-of-sight. The other possible scenario, specifically a larger cloud misaligned with the source would imply a much smoother and slower growth and decrease of the CF, which is not taking place here.

We then assume here the simplest possible geometry that can explain our data, namely the presence of an X-ray source of size (diameter)  $D_s$  and of an obscuring cloud of size  $D_c \leq D_s$ , see Fig. 7. The  $CF$  evolution identifies three different timescales: (i) the crossing time  $t^{(cr)} = 160 \pm 30$  ks, i.e. the total time during which  $CF \neq 0$ ; (ii) the transit time  $t^{(tr)} \leq 26.5$  ks during which the source is maximally covered (i.e. up to 5 intervals are consistent with being maximally covered); (iii) the partially covered rising/decaying time  $t^{(pc)} = (t^{(cr)} - t^{(tr)})/2 = 73.5 \pm 21.5$  ks needed to reach the maximal covering fraction starting from zero (and viceversa). On the other hand all these timescales can be related to the cloud velocity  $v_c$  and cloud/source sizes by  $v_c = D_c/t^{(pc)} = (D_s - D_c)/t^{(tr)} = (D_s + D_c)/t^{(cr)}$ .

**Cloud/source relative sizes** — Since the maximum covering fraction  $CF_{\max} \leq 1$ , the cloud never completely covers the X-ray source (or it may, but only for a time shorter than our bin size of  $\sim 5.3$  ks). The simplest interpretation is that  $D_c = \alpha D_s$  with  $\alpha \leq 1$ . There are two different ways to derive  $\alpha$ . Firstly, as  $CF_{\max} \geq 0.35$ , one has  $\alpha = CF_{\max}^{1/2} \geq 0.59$ . Secondly, as  $(D_s - D_c)/t^{(tr)} = (D_s + D_c)/t^{(cr)}$ , one has  $\alpha = (t^{(cr)} - t^{(tr)})/(t^{(cr)} + t^{(tr)}) = [0.66 - 1]$ . As the two  $\alpha$  must be consistent with each other, we then have that  $\alpha = [0.66 - 1]$ .

**Cloud density/distance** — The combination  $n_c R_c^2$  between cloud density and distance can be estimated from the cloud ionization state  $\xi_c = L_{\text{ion}}/(n_c R_c^2)$  if the overall ionising luminosity  $L_{\text{ion}}$  between 1 and 1000 Ry is known. In the case of SWIFT J2127.4+5654 we have  $L_{\text{ion}} \simeq 2 \times 10^{44}$  erg s $^{-1}$ . We have then repeated our spectral analysis using an ionized absorber (the ZXIPCF model), and we infer that  $\xi_c \leq 20$  erg cm s $^{-1}$  with similar column density as inferred for the neutral model, and with consistent covering fraction evolution (no ionization variability is detected). Hence, we have  $n_c R_c^2 \geq 10^{43}$  cm $^{-1}$ .

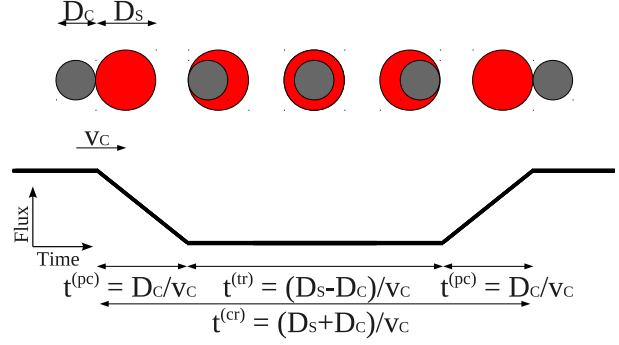


**Figure 7.** The envisaged system geometry. The absorbing cloud (grey) moves with velocity  $v_c$  and partially covers the X-ray source (red in the on-line version). The relevant quantities used in our discussion ( $D_c$ ,  $D_s$ ,  $t^{(pc)}$ ,  $t^{(tr)}$ , and  $t^{(cr)}$ ) are also defined.

We can now use the only relation that has not yet been used, namely  $v_c = D_c/t^{(pc)}$ . Assuming that the cloud transverse velocity is dominated by gravity, and using the relationship between column density, size, and number density, we then have  $(GM_{\text{BH}}/R_c)^{1/2} = D_c/t^{(pc)} = N_{\text{H}}/(n_c t^{(pc)})$ . For a black hole mass of  $M_{\text{BH}} = 1.5 \times 10^7 M_{\odot}$  (as derived from single-epoch optical spectra, see Malizia et al. 2008),  $R_c n_c^{-2} = [1.9 - 3.7] \times 10^{-2}$  cm $^7$ . By combining this result with  $n_c R_c^2 \geq 10^{43}$  cm $^{-1}$  derived above, one has  $n_c^5 \geq 7.3 \times 10^{45}$  cm $^{-15}$ , which then gives  $n_c \geq 1.5 \times 10^9$  cm $^{-3}$  and  $R_c \geq 4.3 \times 10^{16}$  cm.

**Cloud and X-ray source sizes** — The system is now closed, and limits on the cloud and X-ray source sizes can be derived. As  $D_c = N_{\text{H}}/n_c$  one has  $D_c \leq 1.5 \times 10^{13}$  cm =  $7 r_g$ , where we have used a black hole mass of  $1.5 \times 10^7 M_{\odot}$  to define  $1 r_g = 1 GM_{\text{BH}}/c^2 = 2.2 \times 10^{12}$  cm. The upper limit on the cloud size translates into an upper limit on the X-ray emitting region size  $D_s = D_c/\alpha \leq 2.3 \times 10^{13}$  cm =  $10.5 r_g$ .

## 6 SUMMARY AND CONCLUSIONS

We report results from a  $\sim 130$  ks observation of the NLS1 galaxy SWIFT J2127.4+5654 with *XMM-Newton*. We confirm the detection of a relativistically broadened Fe  $K\alpha$  line, originally detected in a previous *Suzaku* observation (Miniutti et al. 2009). All relativistic parameters are consistent with those inferred from the *Suzaku* data. In particular, we confirm an intermediate black hole spin of  $a \sim 0.5$  and a relatively high observer inclination of  $i \sim 44^\circ$ .

The source exhibits significant flux variability throughout the observation and, most importantly, spectral variability is also present during the first 90 ks of the *XMM-Newton* exposure. We perform a time-resolved spectral analysis of the *XMM-Newton* data with the goal of investigating the origin of the observed spectral variability. Our results are consistent with the same baseline spectral model as in the previous *Suzaku* observation (e.g. Miniutti et al. 2009) affected by additional neutral absorption only partially-covering the X-ray source during the first 90 ks of the *XMM-Newton* exposure. Assuming that the spectral variability is driven by changes of the absorber CF, we show that the CF evolution is consistent with one single absorbing structure (cloud) crossing our line-of-sight during the first 90 ks of the exposure.

By considering the first 90 ks of the observation within the framework of a simple source-cloud geometry, we obtain the fol-

lowing constraints on the absorbing cloud: the cloud has a column density of  $N_{\text{H}} = 2.0_{-0.3}^{+0.2} \times 10^{22} \text{ cm}^{-2}$  which, once combined with the estimated cloud density  $n_{\text{c}} \geq 1.5 \times 10^9 \text{ cm}^{-3}$  implies a cloud size (diameter)  $D_{\text{c}} \leq 1.5 \times 10^{13} \text{ cm}$  at a distance from the center of  $R_{\text{c}} \geq 4.3 \times 10^{16} \text{ cm}$ . Assuming that the cloud motion is dominated by gravity the cloud (Keplerian) velocity is then  $v_{\text{c}} \leq 2100 \text{ km s}^{-1}$ . All these properties are consistent with those of a broad-line-region (BLR) cloud partially covering a compact X-ray source during the *XMM-Newton* observation<sup>3</sup>. The excellent agreement between the derived cloud properties and the BLR physical conditions provides further support to our proposed interpretation of the observed X-ray spectral variability.

The partial eclipse can be used to constrain the size of the X-ray emitting region. The *CF* evolution timescales, as well as the maximal observed covering fraction  $CF_{\text{max}}$  imply that the cloud and X-ray emitting region sizes are related through  $D_{\text{c}} = [0.66 - 1] \times D_{\text{s}}$ . The upper limit on the cloud size  $D_{\text{c}} \leq 1.5 \times 10^{13} \text{ cm}$  then translates into an upper limit on the X-ray source size of  $D_{\text{s}} \leq 2.3 \times 10^{13} \text{ cm} = 10.5 r_{\text{g}}/M_{\text{best}}$  where  $M_{\text{best}}$  is the black hole mass in units of  $1.5 \times 10^7 M_{\odot}$ , i.e. the best available estimate of the black hole mass in SWIFT J2127.4+5654 (Malizia et al. 2008). Such a small X-ray emitting region is consistent with previous results based on similar occultation events in the X-rays (Risaliti et al. 2007; 2009) as well as with microlensing results (Dai et al. 2010; Mosquera et al. 2013). A very compact X-ray corona is also consistent with the relatively steep emissivity profile we (and Miniutti et al. 2009) measure for the disc reflection component ( $q \sim 5$ ) which strongly suggests a highly compact X-ray emitting region (e.g. Miniutti & Fabian 2004).

We conclude that we have observed the partial eclipse by a BLR cloud of the X-ray continuum source in SWIFT J2127.4+5654. Our result is in line with the mounting observational evidence that part of the observed X-ray absorption in AGN is due to a clumpy absorber whose properties and location can be identified with either the BLR or with a clumpy torus (in those cases where absorption variability occurs on months to years timescales) which probably are just different part of the same obscuring region. Our analysis strongly suggests that the X-ray continuum is produced in a compact region only a few  $r_{\text{g}}$  in size, which is consistent with the detection of a reflection component off the inner accretion disc. Notice that the relatively high observer inclination we measure from the broad Fe line ( $i \sim 44^\circ$ ) likely enhances the probability of X-ray eclipses (see e.g. Elitzur 2012).

The advent of the next generation of large-collecting area X-ray observatories (e.g. the proposed Athena+ mission, see Nandra et al. 2013 and Dovciak et al. 2013) will allow us to map with even greater accuracy the innermost regions of the accretion flow around accreting black holes via X-ray spectroscopy and X-ray flux and spectral variability studies, including absorption events as the one discussed here (see e.g. Risaliti et al. 2011).

<sup>3</sup> The identification of the absorber with a BLR cloud is also supported by the observed optical broad line FWHM  $\sim 2000 \text{ km s}^{-1}$  (Malizia et al. 2008). By assuming a flattened BLR geometry and the inclination derived from our disc reflection model ( $i = 44^\circ$ ), the FWHM translates into a Keplerian velocity of  $1.4 \times 10^3 \text{ km s}^{-1}$ , which is fully consistent with the cloud velocity upper limit  $v_{\text{c}} \leq 2.1 \times 10^3 \text{ km s}^{-1}$  we derive from our analysis.

## ACKNOWLEDGEMENTS

Based on observations obtained with XMM-Newton, an ESA science mission with instruments and contributions directly funded by ESA Member States and NASA. Financial support for this work was provided by the Spanish MINECO through grant AYA2010-21490-C02-02. The research leading to these results has received funding from the European Union Seventh Framework Programme (FP7/2007–2013) under grant n. 312789. MS thanks CSIC for support through a JAE-Predoc grant. This work was carried out despite the increasingly hostile cutbacks against the Spanish system of science.

## REFERENCES

- Bianchi S., Piconcelli E., Chiaberge M., Jimnez-Bailn E., Matt G. & Fiore F., 2009, *ApJ*, 695, 781B  
 Brenneman, L. W., & Reynolds, C. S. 2006, *ApJ*, 652, 1028  
 Dai X., Kochanek C. S., Chartas G., Kozlowski S., Morgan C.W., Garmire G., Agol E., 2010, *ApJ*, 709, 278  
 Dovciak M. et al., 2013, Supporting paper for the science theme "The Hot and Energetic Universe" to be implemented by the Athena+ X-ray observatory (arXiv:1306.2331)  
 Elitzur, M. 2012, *ApJ Letters*, 747, L33  
 Elvis M., Risaliti G., Nicastro F., Miller J., Fiore F. & Puccetti S., 2004, *ApJ*, 615L, 25E  
 Halpern J.P., 2006, *ATel*, 847, 1  
 Kalberla, P. M. W., Burton, W. B., Hartmann, D., et al. 2005, *A&A*, 440, 775  
 Maiolino R., Risaliti G., Salvati M., Pietrini P., Torricelli-Ciamponi G., Elvis M., Fabbiano G., Braito V. & Reeves J., 2010, *A&A*, 517, 47  
 Malizia A., Bassani L., Bird A. J., Landi R., Masetti N., de Rosa A., Panessa F., Molina M., Dean A. J., Perri M. & Tueller J., 2008, *MNRAS*, 389, 1360  
 Marinucci A., Risaliti G., Wang J., Bianchi S., Elvis M., Matt G. Nardini E. & Braito V., 2013, *MNRAS*, 429, 2581M  
 Miniutti G. & Fabian A. C.,  
 Miniutti G., Panessa F., de Rosa A., Fabian A. C., Malizia A., Molina M., Miller J. M., & Vaughan S., 2009, *MNRAS*, 398, 255  
 Miniutti G., Brandt W. N., Schneider D. P., Fabian A. C., Gallo L. C., Boller Th., 2012, *MNRAS*, 425, 1718  
 Mosquera A. M., Kochanek C. S., Chen B., Dai X., Blackburne J.A., Chartas G., 2013, *ApJ*, 769, 53  
 Nandra K. et al., 2013, Submitted in response to the call for White Papers for the definition of the L2 and L3 missions in the ESA Science program (arXiv:1306.2307)  
 Nenkova M., Sirocky M. M., Nikutta R., Ivezić Ž., Elitzur M. 2008, *ApJ*, 685, 160  
 Patrick A. R., Reeves J. N., Porquet D., Markowitz A. G., Lobban A. P., Terashima Y., 2011, *MNRAS*, 411, 2353  
 Puccetti S., Fiore F., Risaliti G., Capalbi M., Elvis M. & Nicastro F., 2007, *MNRAS*, 377, 607P  
 Reeves, J., Done, C., Pounds, K., et al. 2008, *MNRAS*, 385, L108  
 Risaliti, G., Elvis, M., & Nicastro, F. 2002, *ApJ*, 571, 234  
 Risaliti G., Elvis M., Fabbiano G., Baldi A. & Zezas A., 2005, *ApJ*, 623L, 93R  
 Risaliti G., Elvis M., Fabbiano G., Baldi A., Zezas A. & Salvati M., 2007, *ApJ*, 659L, 111R  
 Risaliti G., Miniutti G., Elvis M., Fabbiano G., Salvati M., Baldi

- A., Braito V., Bianchi S., Matt G., Reeves J., Soria R. & Zezas A., 2009, *ApJ*, 696, 160R
- Risaliti G., Nardini E., Elvis M., Brenneman L., Salvati M., 2011, *MNRAS*, 417, 178
- Ross, R. R., & Fabian, A. C., 2005, *MNRAS*, 358, 211
- Tatum, M. M., Turner, T. J., Sim, S. A., et al., 2012, *ApJ*, 752, 94
- Tueller J. et al., 2005, *ATel*, 669, 1
- Warwick, R. S., Pounds, K. A., & Turner, T. J. 1988, *MNRAS*, 231, 1145
- Zhang T. Z. & Wu X. B., 2002, *ChJAA*, 2, 487Z